Journal of Vacuum Science and Technology A

RESEARCH ARTICLE | JANUARY 29 2024

Composition dependence of intrinsic surface states and Fermi-level pinning at ternary $Al_xGa_{1-x}N$ *m*-plane surfaces

Lars Freter ; Liverios Lymperakis ; Michael Schnedler ; Holger Eisele ; Lei Jin ; Jianxun Liu ; Qian Sun ; Rafal E. Dunin-Borkowski ; Philipp Ebert

J. Vac. Sci. Technol. A 42, 023202 (2024)
https://doi.org/10.1116/6.0003225

JVST A
Journal of Vacuum Science & Technology A

ARTICLE

pubs.aip.org/avs/jva

Composition dependence of intrinsic surface states and Fermi-level pinning at ternary $Al_xGa_{1-x}N$ *m*-plane surfaces

Cite as: J. Vac. Sci. Technol. A 42, 023202 (2024); doi: 10.1116/6.0003225
Submitted: 17 October 2023 · Accepted: 22 December 2023 ·
Published Online: 29 January 2024

Lars Freter,[1] Liverios Lymperakis,[2,3] Michael Schnedler,[1] Holger Eisele,[4] Lei Jin,[1] Jianxun Liu,[5] Qian Sun,[5] Rafal E. Dunin-Borkowski,[1] and Philipp Ebert[1,a)]

AFFILIATIONS

[1]Ernst Ruska-Centrum (ER-C 1) and Peter Grünberg Institut (PGI 5), Forschungszentrum Jülich GmbH, Jülich 52425, Germany
[2]Department of Physics, University of Crete, Heraklion 70013, Greece
[3]Computational Materials Design Department, Max-Planck Institut für Eisenforschung GmbH, Düsseldorf 40237, Germany
[4]Institut für Physik, Otto-von-Guericke-Universität Magdeburg, Universitätsplatz 2, Magdeburg 39106, Germany
[5]Key Laboratory of Nano-devices and Applications, Suzhou Institute of Nano-Tech and Nano-Bionics, Chinese Academy of Sciences (CAS), Suzhou 215123, China

[a)]p.ebert@fz-juelich.de

ABSTRACT

Growth on nonpolar group III-nitride semiconductor surfaces has been suggested to be a remedy for avoiding detrimental polarization effects. However, the presence of intrinsic surface states within the fundamental bandgap at nonpolar surfaces leads to a Fermi-level pinning during growth, affecting the incorporation of dopants and impurities. This is further complicated by the use of ternary, e.g., $Al_xGa_{1-x}N$ layers in device structures. In order to quantify the Fermi-level pinning on ternary group III nitride nonpolar growth surface, the energy position of the group III-derived empty dangling bond surface state at nonpolar $Al_xGa_{1-x}N(10\bar{1}0)$ surfaces is determined as a function of the Al concentration using cross-sectional scanning tunneling microscopy and spectroscopy. The measurements show that the minimum energy of the empty dangling bond state shifts linearly toward midgap for increasing Al concentration with a slope of ≈5 meV/%. These experimental findings are supported by complementary density functional theory calculations.

I. INTRODUCTION

Ternary $Al_xGa_{1-x}N$ alloys are widely used in diverse applications of group III-nitride semiconductors, such as barriers or active media in multiquantum well (MQW)-based light emitting devices,[1] from the visible to far UV spectral range, gate contacts in high power heterojunction field-effect transistors,[2] or strain engineering (buffer) layers of group III nitrides on silicon.[3–6] In many of these devices, polarization changes at heterointerfaces[7] lead to sometimes desired but mostly detrimental effects such as charge separation in active MQW layers or two-dimensional sheet charges in transistors. To avoid unwanted polarization effects, growth on semipolar and nonpolar substrate orientations have been proposed as the solution.[8,9] However, even though nonpolar surfaces are free of polarization charges, intrinsic surface states within the fundamental bandgap of nitride semiconductors[10] give rise to surface potentials with similar disadvantages.[11] For example, Fermi level pinning by the empty Ga-derived dangling bond state on GaN $\{10\bar{1}0\}$ surfaces was found to create a surface potential of ∼0.7 V.[12–21]

However, despite their relevance for device fabrication, so far, only the surface states of GaN,[12,14] InN,[22] and $Al_{0.8}In_{0.2}N$[23] nonpolar surfaces have been thoroughly investigated, while those of other ternary compounds remain unknown. Therefore, we investigate here the composition dependence of intrinsic surface states and Fermi-level pinning at ternary $Al_xGa_{1-x}N$ *m*-plane surfaces by a combination of cross-sectional scanning tunneling microscopy (XSTM) and cross-sectional scanning tunneling spectroscopy (XSTS) as well as density functional theory (DFT) calculations.

II. EXPERIMENT

The investigated sample structure consists of two ternary $Al_xGa_{1-x}N$ layers with step-graded Al contents ($x = 0.17$, 0.35) and thicknesses (370, 320 nm) on top of a 300 nm thick AlN buffer layer. All layers were grown by metal organic chemical vapor phase deposition (MOCVD) on a Si(111) substrate.[24] Secondary ion mass spectrometry (SIMS) indicates a Si dopant concentration in the low 10^{18} cm^{-3} range, without a concentration gradient within each of the three layers.

For the XSTM/XSTS investigations, small rectangular samples were cut from the as-grown wafer, thinned, and electrically contacted (using sputtered Au layers).[24] After transfer into an ultrahigh vacuum chamber ($p < 2 \times 10^{-8}$ Pa), the samples were cleaved to obtain contamination-free cross-sectional $(10\bar{1}0)$ surfaces. The XSTM and XSTS measurements were performed without interruption of the vacuum, using electro-chemically etched tungsten tips.

Compositions and layer thicknesses were studied by energy dispersive x-ray (EDX) spectroscopy in a FEI Titan G2 80-200 CREWLEY scanning transmission electron microscope (STEM).[24,25] Since the measured and nominal ternary (Al,Ga)N compositions are very close considering the measurement accuracy, we use the nominal compositions for labeling the layers in the following.

III. RESULTS

Figure 1 provides a microscopic, electronic, and chemical overview of the $Al_{0.17}Ga_{0.83}N/Al_{0.35}Ga_{0.65}N/AlN/Si$ heterostructure. The constant-current XSTM image in Fig. 1(a) illustrates the topography of the nonpolar $(10\bar{1}0)$ cleavage surface in a cross-sectional view through the heterostructure. The topography is characterized by large atomically flat terraces separated by cleavage steps of various heights with a density of $(3–5)\times10^4$ cm^{-1}. At the heterointerfaces, no change in topography can be discerned, despite the rather large compositional changes [cf. Fig. 1(c)]. In particular, the cleavage steps cross the interfaces without any directional change. Only in the far left bottom corner of the constant-current STM image, the outermost edge of the Si substrate, which is not of interest here, induces a change in cleavage orientation and subsequently, a large height change.

Current imaging tunneling spectroscopy (CITS) maps evaluated at negative sample voltages (not shown here) reveal no detectable electronic contrast change at the $Al_{0.35}Ga_{0.65}N/AlN$ and $Al_{0.17}Ga_{0.83}N/Al_{0.35}Ga_{0.65}N$ heterointerfaces. In contrast, CITS maps evaluated at positive sample voltages [Fig. 1(b)] reveal a notable change of current-induced contrast at the $Al_{0.35}Ga_{0.65}N/AlN$ interface (cf. left dashed white line), whereas the electronic change at the $Al_{0.17}Ga_{0.83}N/Al_{0.35}Ga_{0.65}N$ interface with smaller composition change is almost absent. Therefore, we determined the spatial position of this latter $Al_{0.17}Ga_{0.83}N/Al_{0.35}Ga_{0.65}N$ interface in the XSTM image and CITS map using the $Al_{0.35}Ga_{0.65}N$ layer thickness as obtained by EDX (cf. right white dashed lines), relative to the $Al_{0.35}Ga_{0.65}N/AlN$ interface position identified in the CITS maps.

Note, the curved stripe contrast within the (Al,Ga)N layers are step-related features attributable to step-induced states, whereas the horizontal single pixel wide lines arise from tip-instabilities.

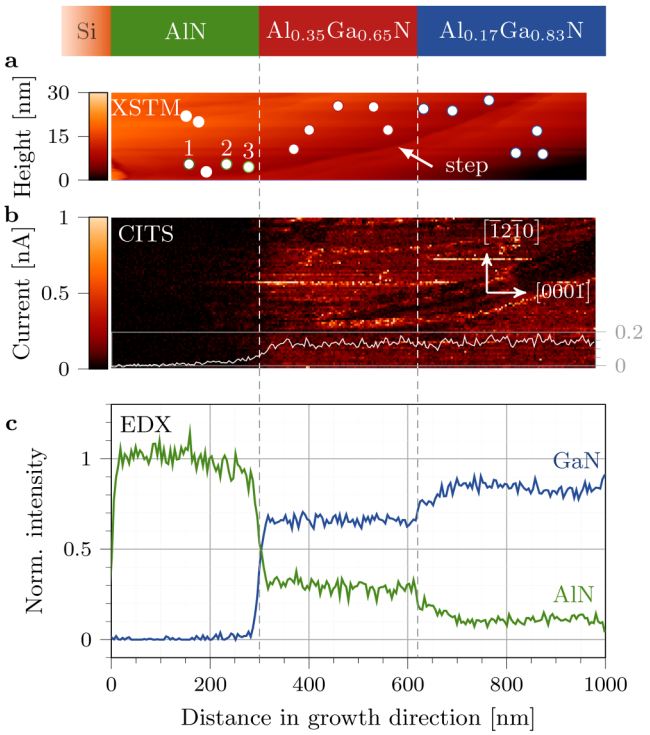

FIG. 1. (a) Constant-current XSTM image, measured at a setpoint of −2.5 V and 80 pA, revealing atomic terraces separated by steps. The white dots correspond to the acquisition positions of sets of 25 tunneling spectra each used in Fig. 2. (b) CITS map acquired in an adjacent area. The CITS map depicts the measured current at a selected voltage of +4.8 V. The tip-sample separation is fixed by a setpoint of −4.5 V and 80 pA. The white overlay in the bottom region shows a line profile in the [0001] direction of the current in nA (right scale) at a voltage of +4.8 V extracted from the CITS map. (c) Al and Ga composition profiles along the [0001] growth direction measured by EDX taken from Ref. 24, revealing the interface positions between the three layers of interest. While the XSTM image in (b) does not reveal topographic changes at the heterointerfaces, the CITS image in (c) exhibits a pronounced (vanishing) change of contrast and thus of the electronic properties at the $Al_{0.35}Ga_{0.65}N/AlN$ ($Al_{0.17}Ga_{0.83}N/Al_{0.35}Ga_{0.65}N$) interface.

At this stage, we turn to current-voltage spectra acquired at different spatial positions on the cross-sectional cleavage surface marked by filled circles in Fig. 1(a). Figures 2(a) and 2(b) show averages of all tunneling spectra acquired at spatial positions within the $Al_{0.17}Ga_{0.83}N$ and $Al_{0.35}Ga_{0.65}N$ layers, far enough from the interfaces, in blue and red symbols, respectively. The error bars reveal that the spectra and the electronic properties are homogeneous throughout each (Al,Ga)N layer. In contrast, within the AlN layer, the tunneling spectra exhibit a pronounced dependence along the growth direction. This is illustrated with three averaged spectra, acquired within the AlN layer but with increasing distances from the $Al_{0.35}Ga_{0.65}N/AlN$ interface in Fig. 2(c). Their spatial positions are numbered correspondingly as in Fig. 1(a).

Figure 2 illustrates that the negative voltage branches of all spectra of the three layers exhibit identical onset voltages and slopes,

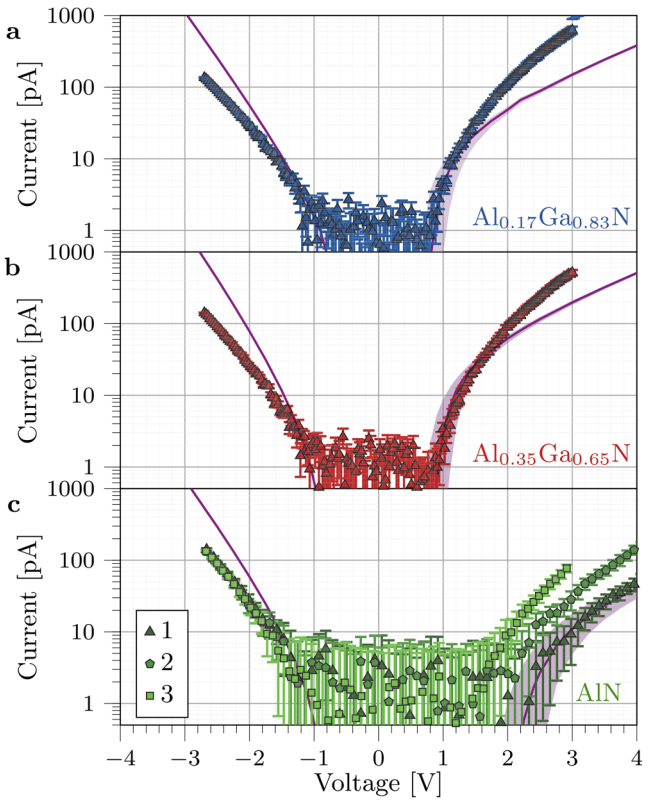

FIG. 2. Current-voltage $I(V)$ tunnel spectra measured on (a) the $Al_{0.17}Ga_{0.83}N$ layer (triangles), (b) the $Al_{0.35}Ga_{0.65}N$ layer (triangles), and (c) the AlN layer at three different spatial positions visible in Fig. 1(a) (shown as triangles, pentagons, and squares). All spectra were obtained using the same setpoint (−2.5 V and 80 pA). The onset of the spectra fitted by adjusting the surface state energy level in the simulation as described in the text 26–28 (lines). The shading illustrates the range induced by a ±0.2 and ±0.4 eV change of the surface state position of (Al,Ga)N and AlN, respectively.

in line with the lack of any contrast at the interfaces in filled states images [see Fig. 1(a)]. In contrast, at positive voltages, the onsets increase with the Al concentration, whereas the slope decreases.

Within the AlN layer, a rather large systematic change of the spectra occurs in addition: The AlN spectra exhibit a shift to larger onset voltages with increasing distance to the $Al_{0.35}Ga_{0.65}N$/AlN interface [cf. Fig. 2(c)]. Therefore, we first consider in the discussion below spectra measured in the center of the AlN layer, i.e., far away from the AlN/$Al_{0.35}Ga_{0.65}N$ interface [triangles in Fig. 2(c)]. Later on, we address the systematic shifts. The two ternary (Al,Ga)N layers exhibit no such spatial variation of the tunneling spectra.

IV. DISCUSSION

A. Surface band bending

In order to understand the Al composition-dependent current onsets at positive voltages (and the lack of Al concentration dependence at negative voltages), we recall that clean GaN(10$\bar{1}$0) surfaces exhibit filled dangling bonds localized at the surface N atoms and empty dangling bonds above the surface Ga atoms. Both types of dangling bonds point into the vacuum.[12] Unlike nonpolar surfaces of zincblende III–V semiconductors, where all surface states are found to be outside of the fundamental bandgap,[29] the empty Ga-derived dangling bond of GaN(10$\bar{1}$0) is energetically located in the upper part of the fundamental bandgap.[12–21]

The presence of the empty dangling bond state within the bandgap induces an upward band bending and becomes partially occupied on *n*-type surfaces. Due to the high density of the Ga-derived surface state, its lowermost tail of the LDOS in the bandgap is pinned at the Fermi level (the so-called Fermi-level pinning). Hence, the magnitude of the band bending reflects the energy separation between the minimum of the surface state and the conduction band edge in highly *n*-doped GaN. Note, the density of step states can be estimated to about 10^{12} cm^{-2} on the basis of the measured step density. This value is much lower than the density of intrinsic surface states of 6.2×10^{14} cm^{-2}, which thus dominates Fermi-level pinning.

In a XSTM setup, the additional presence of a biased probe tip modifies this intrinsic band bending: At positive voltages, this additional electric field increases the intrinsic band bending primarily at large voltages only, where the tip-induced band bending dominates. At small positive voltages, the tip-induced band bending is negligible and, therefore, only the intrinsic band bending due to the partial occupation of the minimum of the empty surface state in the bandgap (i.e., Fermi-level pinning) governs the tunnel current onset.[15] Thus, the onset of the positive voltage branch of the $I(V)$ curves is indicative of the position of the intrinsic surface state in the bandgap.[15]

At negative voltages, the tip attempts to induce a downward band bending. However, the density of the Ga-derived surface state is too large, and, therefore, the partially occupied surface state cannot be fully filled. Hence, the Fermi-level pinning at the Ga-derived surface state energy prevails. As outlined previously, this is apparently in conflict with the onset of the negative current branch.[15] The apparent conflict can be resolved by considering the tunneling currents themselves. Under tunneling conditions with negative sample voltages applied, the electrons tunnel from the partially filled Ga-derived surface state into the tip states. Due to the particular electronic structure of the conduction band minimum and the Ga-derived surface state, the electrons from the conduction band cannot refill the surface state at a sufficient rate.[15] Hence, under tunneling conditions, the surface state is emptied and does not influence the tip-induced band bending. Instead, the conduction band edge is dragged below the Fermi energy, creating an electron accumulation zone in the conduction band. This accumulation zone is at the origin of the strong tunnel current into the tip starting already at small negative sample voltages. The accumulation current is independent of the energy position of the surface state.

For the ternary $Al_{0.17}Ga_{0.83}N$ and $Al_{0.35}Ga_{0.65}N$ (10$\bar{1}$0) cleavage surfaces, an analogous surface structure is obtained by theory (see calculations below). Hence, the tunnel current onsets can be interpreted on the basis of the accumulation current (negative current branch) and the energy position of the cation-derived dangling bond state in the bandgap (positive current branch).

The onset of the accumulation current is in the first approximation solely determined by the energy difference between the Fermi level and the conduction band minimum. Since all layers in the heterostructure are *n*-doped, they will have almost identical Fermi level positions with respect to the conduction band, and thus, the resulting current and its onset can be anticipated to be essentially independent of the Al composition. Thus, the contrast of filled state images is dominated by topographic features only, explaining the lack of electronic contrast at the heterointerfaces in the XSTM images acquired at negative voltages.

B. Simulation of the tunnel current

1. $Al_xGa_{1-x}N$ layers

Based on the electronic surface structure and tunneling model, we simulated the tunnel currents of the two ternary $Al_{0.17}Ga_{0.83}N$ and $Al_{0.35}Ga_{0.65}N$ $(10\bar{1}0)$ cleavage surfaces. For the simulation of the tunnel currents, the relevant material parameters of the ternary alloys (electron affinity and dielectric constant) were approximated by Vegard's law from the binary compounds. The effective mass and the donor ionization energy were approximated by the values of GaN since in the used composition range, almost no changes occur.[30–34] The Si doping concentration in both ternary layers was estimated on the basis of SIMS data to 1.6×10^{18} cm^{-3} under the assumption of no doping compensation.[33–35]

The minimum of the empty cation-derived surface state's local density of states (LDOS) is modeled as Gaussian distribution with a full width at half maximum of 0.1 eV and a surface state density of 6×10^{14} cm^{-2}. Note, only the lowermost tail below the Fermi level is occupied, yielding a surface charge density in the range of 10^{12}–10^{13} cm^{-2}. The centroid energy of the Gaussian distribution E_{pin} was used as fit parameter and represents the minimum of the surface state's LDOS. Note, since only the lowermost DOS of the surface state is populated and thereby inducing the Fermi-level pinning, it is sufficient to include only this lowermost DOS in the electrostatic calculation. The higher states of the dispersing surface state extend into the conduction band but are not relevant for Fermi-level pinning. A standard probe tip with a 60 nm radius, an apex opening angle of 45°, and a work function of 4.0 eV[36–39] was used in all simulations. The electron affinities of the ternary compounds are determined on the basis of the respective values of the binary compounds using Vegard's law, since an almost linear dependence of the electron affinity on the Al composition has been observed.[40–42] For the nonpolar GaN$(10\bar{1}0)$ surface an experimental value of 4.1 eV is used.[43] For the nonpolar AlN$(10\bar{1}0)$ surface, no experimental data are available, and we turned to theoretical calculations, which yielded an electron affinity 2.3 eV smaller than that of GaN$(10\bar{1}0)$. This is compatible with the values in the upper range of the electron affinity for polar AlN surfaces of 0.6 to 2.0 eV.[40,41,44–48] Thus, electron affinities of $\chi = 3.74$ and 3.37 eV are used for the two ternary $Al_{0.17}Ga_{0.83}N$ and $Al_{0.35}Ga_{0.65}N$ $(10\bar{1}0)$ cleavage surfaces, respectively.

The violet solid lines in Fig. 2 show the best agreeing simulated tunnel spectra in comparison to the measured $I(V)$ curves. In the case of the ternary nitride layers, the best agreement is achieved for minima of the empty surface state of $E_C-(0.7 \pm 0.2)$ eV and $E_C-(0.8 \pm 0.2)$ eV for Al contents of 17%, and 35%, respectively.

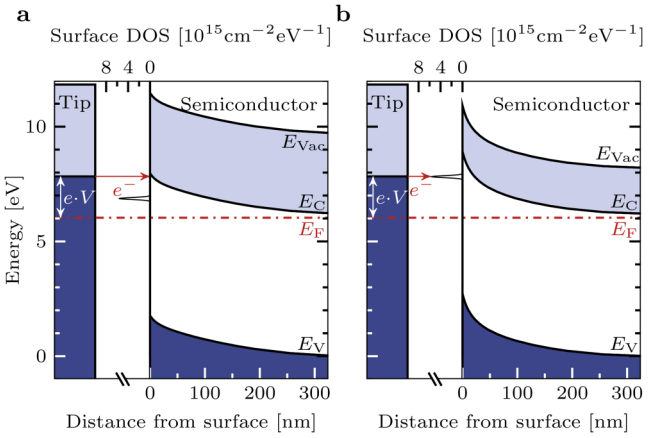

FIG. 3. Band diagrams for (a) tunneling only into bulk states (at large electron affinity) and (b) tunneling into the minimum of the empty surface state (at small electron affinity) illustrated for the onset voltage of the positive current branch. Note tunneling at onset voltages occurs only in the minimum of the empty surface state, which is, therefore, illustrated as Gaussian in the first approximation.

The violet shaded areas in Fig. 2 indicate the range of the simulated $I(V)$ curves that correspond to the respective uncertainties.

2. AlN layer

At this stage, we turn to the pure AlN$(10\bar{1}0)$ surface. First, we assume that the electronic structure, in terms of the presence and local density of states' decay into the vacuum of the empty surface state in bandgap, and its effect on the tunnel current of the AlN$(10\bar{1}0)$ surface are analogous to those of the (Al,Ga)N and GaN $(10\bar{1}0)$ surfaces. Assuming this model, we simulate the tunnel current in the center of the AlN layer, farthest away from any interface, using the same procedure as outlined above for the ternary surfaces with adjusted materials parameter.

For pure AlN, the actual carrier concentration is significantly smaller than the Si doping concentrations due to compensation[33–35,49–52] and a sharp increase in the activation energy for higher Al concentrations, reaching 250 meV for pure AlN.[33,34] To take this effect into account, a doping concentration as low as 1×10^{16} cm^{-3} was assumed.

The such simulated AlN tunnel spectrum is shown as a violet line in Fig. 2(c) and the respective band diagram in Fig. 3(a). For this simulation, the surface state position and the electron affinity are used as fit parameters. The simulation reproduces well the onsets and slopes at positive and negative voltages. The onset at positive voltages is directly connected to the energy position of the empty surface state of E_C-1.4 ± 0.4 eV.

However, the electron affinity needed for a reasonable agreement is rather large with 3.5 eV as compared to literature values ranging between 0.6 and 2 eV.[40,41,44–48] Smaller electron affinities lead to much too large slopes of the negative tunnel current branch, due to the reduced tunneling barrier. Simultaneously, a lower electron affinity

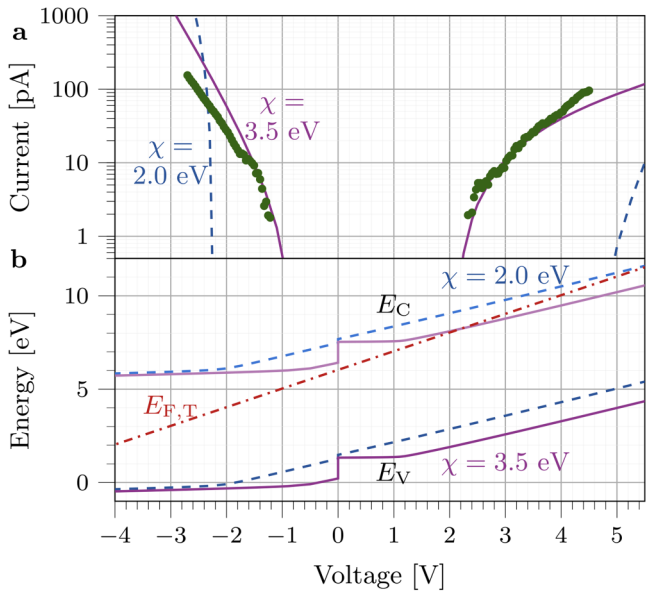

FIG. 4. (a) Comparison of the $I(V)$ tunnel spectrum measured in the center of the AlN layer [spectrum number 1 in Fig. 2(c)] with simulated spectra assuming tunneling into bulk states only (and a doping concentration of 1×10^{16} cm^{-3}). Two calculations are illustrated, which use electron affinities of $\chi = 2.0$ eV and $\chi = 3.5$ eV. (b) Simulated positions of the conduction (E_C) and valence (E_V) band edges at the surface as a function of applied voltage at the AlN surface for the two cases [see (a)]. The Fermi level of the tip (dashed-dotted line) is for low electron affinities inside the fundamental bandgap for almost the whole simulated voltage range. At high electron affinities, the Fermi level of the tip crosses the conduction band edge at roughly +2 V. The offset at 0 V is model based, since at negative voltages the surface state is almost instantaneously emptied and cannot be refilled. Thus, the upward band bending (or Fermi-level pinning) due to the surface state cannot be maintained. The subtle kinks in the band edges at +1 V arise from the charging/discharging of the surface state due to tip-induced upward band bending.

shifts the current onsets to larger absolute voltages due to a much larger contact potential between the tip and the AlN surface. Figure 4(a) illustrates this situation for an exemplary electron affinity of 2 eV. Note, ultimately, the Fermi level of the tip faces only energies within the fundamental bandgap of AlN [Fig. 4(b)] and thus no states are present in the sample for elastic tunneling to tip states. This suppresses tunneling and results in a too wide apparent bandgap, which is limited at negative voltages by tunneling from a tip-induced accumulation zone in the AlN conduction band and at positive voltages by the crossing of the tip's Fermi level with the conduction band edge.

Therefore, we turn to an alternative tunneling model based on tunneling directly into and out of the AlN surface states. Since the filled and empty dangling bond surface states are in the fundamental bandgap, the surface's bandgap is effectively smaller and thus tunneling of electrons between the tip and the surface states becomes possible at much smaller voltages than tunneling into bulk states [see Fig. 3(b)]. The onset voltage V_{onset} of tunneling into the empty dangling bond surface state is a function of the surface state's minimum energy position relative to the conduction band ($E_C - E_{SS}$) and the band bending at the surface (ϕ_{surf}),

$$E_C - E_{SS} = e(\phi_{surf} - V_{onset}). \quad (1)$$

Using this model, $E_C - E_{SS}$ can be deduced from the current onset measured in the experimental $I(V)$ spectra, provided that the surface band bending at the onset voltage is known. Since ϕ_{surf} is not directly accessible in XSTS experiments, it is calculated by solving the electrostatic potential of the tip-vacuum-semiconductor system.[26–28]

The onset voltage of the positive current branch V_{onset} is experimentally extracted by fitting an exponential function $I \propto \exp(\alpha \cdot |V - V_{onset}|^{0.5})$ to the current values $I(V)$. This yields $V_{onset} = +1.8$ V, which results into a surface state energy below the conduction band edge of $E_C - E_{SS} = (1.1 \pm 0.4)$ eV for AlN $(10\bar{1}0)$. The error bar is estimated on the basis of the accuracy of the determination of V_{onset} and a range of tip radii used in the calculation.[53] The calculations were done assuming a electron affinity of 2 eV for AlN as outlined above. If the electron affinity is smaller (e.g., 1.5 eV), the resulting surface state energy increase slightly (e.g., from 1.1 to 1.5 eV).

It is worth noting that dislocations intersect the m-plane cleavage surface of the different (Al,Ga)N layers, with decreasing concentrations along the growth direction. The dislocation cores can be anticipated to exhibit defect states in the bandgap too. However, the density of dislocations is many orders of magnitude smaller than the density of intrinsic surface states.[24] Hence, the effect of dislocation states or their strain field can be neglected.

C. Comparison with DFT calculations

We now turn to a comparison with DFT calculations. For our DFT calculations with the Vienna Ab-initio Simulation Package (VASP),[55,56] we used the Heyd, Scuseria, and Ernzerhof hybrid functional with a mixing parameter a of 0.25 (HSE06),[57] projector augmented wave (PAW) potentials[58] and a planewave energy cutoff of 400 eV. Convergence with respect to energy cutoff, vacuum, and slab thickness was explicitly checked and found to provide surface energies with an accuracy better than 5 meV/1 × 1. The Brillouin zone (BZ) was sampled using an equivalent $4 \times 4 \times 3\,\Gamma$ centered Monkhorst–Pack k-point mesh for the bulk primitive unit cell. The calculated fundamental bandgaps ($E_C - E_V$) of binary bulk GaN and AlN are 3.09 and 5.59 eV, respectively.

With this methodology a total of six distinct AlGaN alloy compositions were computed. For each composition, different configurations in a 16 atoms supercell having the primitive vectors along $\langle 1\bar{1}00\rangle$, $\langle 11\bar{2}0\rangle$, and $\langle 0001\rangle$ have been constructed. The positions of the atoms were relaxed until all forces were less than 0.01 eV/Å. The lattice constants were determined by applying Vegard's law, i.e., varied linearly with the composition. For the end constituents, the equilibrium lattice constants have been used.

To model the surfaces, the bulk supercells were repeated along the $\langle 1\bar{1}00\rangle$ axis, and slabs with 16 MLs thickness were constructed. For each configuration, the bulk was cleaved at four different planes to model different surface alloy configurations for the same composition and bulk configuration. The anion and cation dangling bonds at the bottom side of the slab were passivated by

partially charged pseudohydrogens. Atoms in the four topmost layers were allowed to relax.

Figure 5 depicts the minimum of the cation-derived surface state relative to the bulk conduction band edge ($E_C - E_{SS}$) as obtained by the DFT calculations and experimentally. The surface state position obtained in DFT calculations is indicated by red circles. For pure GaN, the minimum of the surface state is calculated to be 0.1 eV below the bulk conduction band minimum. For higher Al contents, the difference between the bulk conduction band edge and the minimum of the surface state increases until it reaches ≈ 1.2 eV for pure AlN. The experimentally obtained values are depicted as filled and empty diamonds for tunneling into bulk and surface states, respectively. The values found in literature for pure GaN[12,15,20] and AlN[54] are shown as brown pentagons in Fig. 5.

The present DFT calculations overestimate the position of the dangling bond surface state with respect to the bulk valence band maximum (≈3 eV) (i.e., underestimate the energy difference between the empty dangling bond state and the bulk conduction band minimum) compared to previous reports: Both LDA+U[55] and LDA based modified pseudopotential[56] calculations predict the empty surface state at ≈ 2.7 eV above the bulk VBM. This difference can be attributed to the different methodologies and the alignment between the ternary alloys and AlN needed in the present case.

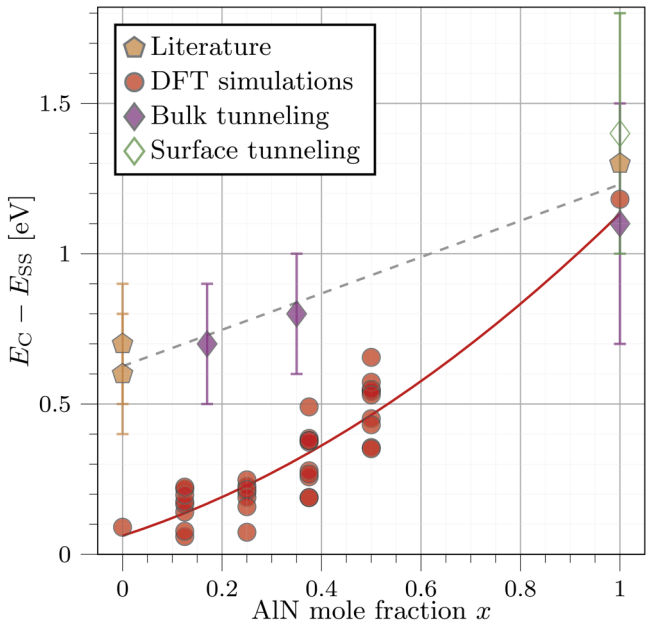

FIG. 5. Energy of the minimum of the empty cation-derived surface dangling bond state relative to the conduction band edge for different Al compositions x of $Al_xGa_{1-x}N(10\bar{1}0)$ surfaces. The circles represent results from our DFT calculations. The filled (empty) diamonds correspond to the surface state positions obtained from the measured tunneling spectra using simulation assuming tunneling into bulk bands only (tunneling into surface states of AlN only). Pentagons represent literature values extracted from Refs. 12, 15, and 20 for GaN and from Ref. 55 for AlN.

The errors in the experimental values for the energy minima of the surface state are primarily of statistical nature arising from the noise during the acquisition of the tunneling spectra (see error bars in Fig. 2): The errors of the extracted surface state energy minima in Fig. 5 were derived by comparing the confidence range of the simulation (determined using variations of the surface state position in the simulation) with the experimental error bar range of the tunneling spectra (in Fig. 2). Agreement of both ranges yielded the final error bars in Fig. 5.

Hence, the calculated literature value for pure AlN and the present DFT calculation are in good agreement and fit well with the surface state position determined experimentally here. Therefore, both the surface state position resulting from measurement and the one resulting from DFT calculation are in good agreement and reveal a weak shift of the surface state toward midgap with increasing Al concentration (and thus of the surface potential) of roughly 5×10^{-3} eV/%. This trend is indicated by the gray dashed line in Fig. 5.

D. Spatial gradient of AlN electronic properties

Finally, we address the spatial dependence of the tunneling spectra within the AlN layer. Figure 6 illustrates the tunnel current in false colors vs voltage and spatial position. The current onsets appear as dark-bright color transition at both voltage polarities. Within the ternary (Al,Ga)N layers little changes occur. However, at the transition from the $Al_{0.35}Ga_{0.65}N$/AlN interface the current onset increases at positive voltages continuously within the AlN

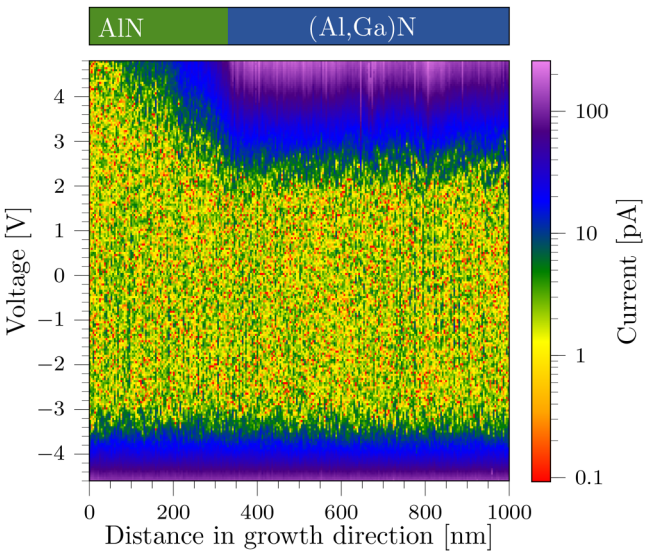

FIG. 6. Evolution of tunnel spectra across the $Al_xGa_{1-x}N$/AlN interface along the growth direction: The spectra were measured using a negative setpoint of −4.5 V and 80 pA. The bright to dark color transitions at positive and negative voltages correspond to the respective current onsets, revealing the apparent bandgap. A wide transition region of the positive current onset and thereby apparent bandgap between AlN and (Al,Ga)N is visible.

layer over a spatial extension of roughly 150 nm. This effect is in line with the shifting positive current branches in Fig. 2(c).

In order to identify the origin of the changes of the tunneling spectra within the AlN layer, we checked possible compositional fluctuations using SIMS. Except Ga, no other element is found to have a concentration decay within the AlN layer. However, the highest Ga concentration within the AlN layer is smaller than 1% according to SIMS data and smaller than about 3% estimated on the basis of the EDX data (Fig. 1). At these concentrations, the conductivity and free carrier density is not changing sufficiently to account for the changes in tunneling spectroscopy observed within the AlN layer.[51,59] Thus, Ga/Al interdiffusion can be ruled out as the origin.

The spatial extension of the current onsets within the AlN of roughly 150 nm coincides, however, with the screening length within the AlN bulk visible in Fig. 3(b). This suggests that the spatial variation reflects the screening of the build-in potential at the $Al_{0.35}Ga_{0.65}N$/AlN interface and the different carrier concentrations in both layers.

V. CONCLUSION

We unravel the energy position of the group III-derived empty dangling bond surface state at nonpolar $Al_xGa_{1-x}N(10\bar{1}0)$ surfaces as a function of the Al concentration using cross-sectional scanning tunneling spectroscopy in conjunction with tunnel current simulations. The measurements show that the minimum energy of the empty dangling bond state shifts toward midgap with increasing Al concentration. The shift is in first approximation linear with a slope of ≈ 5 meV/%. These experimental findings are in good agreement with complementary DFT calculations, which reveal the same trend.

ACKNOWLEDGMENTS

This work was funded by the Deutsche Forschungsgemeinschaft (DFG, German Research Foundation) (Grant No. 398305088). The authors thank Y. Wang, L. Zhang, and V. Assenmacher for their help with the experiments.

AUTHOR DECLARATIONS

Conflict of Interest

The authors have no conflicts to disclose.

Author Contributions

Lars Freter: Formal analysis (equal); Investigation (equal); Visualization (equal); Writing – original draft (equal). **Liverios Lymperakis:** Investigation (equal); Writing – review & editing (equal). **Michael Schnedler:** Investigation (equal); Software (equal); Writing – review & editing (equal). **Holger Eisele:** Funding acquisition (equal); Writing – review & editing (equal). **Lei Jin:** Investigation (equal). **Jianxun Liu:** Resources (equal); Writing – review & editing (equal). **Qian Sun:** Resources (equal); Writing – review & editing (equal). **Rafal E. Dunin-Borkowski:** Validation (equal). **Philipp Ebert:** Funding acquisition (equal); Investigation (equal); Supervision (equal); Writing – review & editing (equal).

DATA AVAILABILITY

The data that support the findings of this study are available from the corresponding author upon reasonable request.

REFERENCES

[1]A. I. Alhassan, R. M. Farrell, B. Saifaddin, A. Mughal, F. Wu, S. P. DenBaars, S. Nakamura, and J. S. Speck, Opt. Express **24**, 17868 (2016).
[2]T. Fujiwara, S. Rajan, S. Keller, M. Higashiwaki, J. S. Speck, S. P. DenBaars, and U. K. Mishra, Appl. Phys. Express **2**, 011001 (2009).
[3]A. Dadgar *et al.* , Phys. Status Solidi C **0**, 1583 (2003).
[4]Y. Sun *et al.* , Nat. Photonics **10**, 595 (2016).
[5]R. Xiang *et al.* , J. Alloys Comp. **509**, 2227 (2011).
[6]J. Cheng *et al.* , Sci. Rep. **6**, 23020 (2016).
[7]C. E. Dreyer, A. Janotti, C. G. Van de Walle, and D. Vanderbilt, Phys. Rev. X **6**, 021038 (2016).
[8]P. Waltereit, O. Brandt, A. Trampert, H. T. Grahn, J. Menniger, M. Ramsteiner, M. Reiche, and K. H. Ploog, Nature **406**, 865 (2000).
[9]V. N. Bessolov, E. V. Konenkova, S. A. Kukushkin, A. V. Osipov, and S. N. Rodin, Rev. Adv. Mat. Sci. **38**, 75 (2014).
[10]V. Bermudez, Surf. Sci. Rep. **72**, 147 (2017).
[11]L. Janicki, J. Misiewicz, G. Cywiński, M. Sawicka, C. Skierbiszewski, and R. Kudrawiec, Appl. Phys. Express **9**, 021002 (2016).
[12]L. Lymperakis *et al.* , Appl. Phys. Lett. **103**, 152101 (2013).
[13]M. Himmerlich, A. Eisenhardt, S. Shokhovets, S. Krischok, J. Räthel, E. Speiser, M. D. Neumann, A. Navarro-Quezada, and N. Esser, Appl. Phys. Lett. **104**, 171602 (2014).
[14]M. Landmann, E. Rauls, W. G. Schmidt, M. D. Neumann, E. Speiser, and N. Esser, Phys. Rev. B **91**, 035302 (2015).
[15]M. Schnedler, V. Portz, H. Eisele, R. E. Dunin-Borkowski, and P. Ebert, Phys. Rev. B **91**, 205309 (2015).
[16]S. Nayak, M. H. Naik, M. Jain, U. V. Waghmare, and S. M. Shivaprasad, J. Vac. Sci. Technol. A **38**, 063205 (2020).
[17]X. Cai, Y. Ma, J. Ma, D. Xu, and X. Luo, Phys. Chem. Chem. Phys. **23**, 5431 (2021).
[18]K. Sagisaka, O. Custance, N. Ishida, T. Nakamura, and Y. Koide, Phys. Rev. B **106**, 115309 (2022).
[19]L. Lymperakis, J. Neugebauer, M. Himmerlich, S. Krischok, M. Rink, J. Kröger, and V. M. Polyakov, Phys. Rev. B **95**, 195314 (2017).
[20]C. G. Van de Walle and D. Segev, J. Appl. Phys. **101**, 081704 (2007).
[21]L. Janicki *et al.* , Jap. J. Appl. Phys. **55**, 05FA08 (2016).
[22]H. Eisele *et al.* , Phys. Rev. B **94**, 245201 (2016).
[23]V. Portz *et al.* , Appl. Phys. Lett. **110**, 022104 (2017).
[24]L. Zhang, V. Portz, M. Schnedler, L. Jin, Y. Wang, X. Hao, H. Eisele, R. E. Dunin-Borkowski, and P. Ebert, Philos. Mag. **98**, 3072 (2018).
[25]A. Kovács, R. Schierholz, and K. Tillmann, J. Large-Scale Res. Facil. **2**, A43 (2016).
[26]M. Schnedler, V. Portz, P. H. Weidlich, R. E. Dunin-Borkowski, and P. Ebert, Phys. Rev. B **91**, 235305 (2015).
[27]M. Schnedler, R. E. Dunin-Borkowski, and P. Ebert, Phys. Rev. B **93**, 195444 (2016).
[28]M. Schnedler, P_SpaceChargeLight (2021), see https://github.com/mschnedler/P_SpaceChargeLight (accepted June 2021).
[29]J. R. Chelikowsky and M. L. Cohen, Phys. Rev. B **20**, 4150 (1979).
[30]W. Götz, N. M. Johnson, C. Chen, H. Liu, C. Kuo, and W. Imler, Appl. Phys. Lett. **68**, 3144 (1996).
[31]C. G. Van de Walle, C. Stampfl, and J. Neugebauer, J. Cryst. Growth **189-190**, 505 (1998).
[32]H. Wang and A.-B. Chen, J. Appl. Phys. **87**, 7859 (2000).
[33]R. Collazo, S. Mita, J. Xie, A. Rice, J. Tweedie, R. Dalmau, and Z. Sitar, Phys. Status Solidi C **8**, 2031 (2011).
[34]I. S. Bryan, "Al-rich AlGaN and AlN growth on bulk AlN single crystal substrates," Ph.D. thesis (North Carolina State University, 2015).

[35]I. Bryan *et al.* , Appl. Phys. Lett. **112**, 062102 (2018).
[36]K. Besocke and H. Wagner, Phys. Rev. B **8**, 4597 (1973).
[37]C. J. Fall, N. Binggeli, and A. Baldereschi, Phys. Rev. B **65**, 045401 (2001).
[38]S. Loth, M. Wenderoth, R. G. Ulbrich, S. Malzer, and G. H. Döhler, Phys. Rev. B **76**, 235318 (2007).
[39]A. P. Wijnheijmer, J. K. Garleff, M. A. V. D. Heijden, and P. M. Koenraad, J. Vac. Sci. Technol. B **28**, 1086 (2010).
[40]T. Kozawa, T. Mori, T. Ohwaki, Y. Taga, and N. Sawaki, Jpn. J. Appl. Phys. **39**, L772 (2000).
[41]S. P. Grabowski, M. Schneider, H. Nienhaus, W. Mönch, R. Dimitrov, O. Ambacher, and M. Stutzmann, Appl. Phys. Lett. **78**, 2503 (2001).
[42]P. Reddy, I. Bryan, Z. Bryan, J. Tweedie, S. Washiyama, R. Kirste, S. Mita, R. Collazo, and Z. Sitar, Appl. Phys. Lett. **107**, 091603 (2015).
[43]V. Portz, M. Schnedler, H. Eisele, R. E. Dunin-Borkowski, and P. Ebert, Phys. Rev. B **97**, 115433 (2018).
[44]V. M. Bermudez, T. M. Jung, K. Doverspike, and A. E. Wickenden, J. Appl. Phys. **79**, 110 (1996).
[45]C. I. Wu, A. Kahn, E. S. Hellman, and D. N. E. Buchanan, Appl. Phys. Lett. **73**, 1346 (1998).
[46]C. I. Wu and A. Kahn, Appl. Phys. Lett. **74**, 546 (1999).
[47]P. G. Moses, M. Miao, Q. Yan, and C. G. Van de Walle, J. Chem. Phys. **134**, 084703 (2011).
[48]P. Strak, P. Kempisty, K. Sakowski, and S. Krukowski, J. Vac. Sci. Technol. A **35**, 021406 (2017).
[49]Y. Taniyasu, M. Kasu, and N. Kobayashi, Appl. Phys. Lett. **81**, 1255 (2002).
[50]Y. Shimahara, H. Miyake, K. Hiramatsu, F. Fukuyo, T. Okada, H. Takaoka, and H. Yoshida, Jpn. J. Appl. Phys. **50**, 095502 (2011).
[51]F. Mehnke *et al.* , Appl. Phys. Lett. **103**, 212109 (2013).
[52]J. S. Harris *et al.* , Appl. Phys. Lett. **112**, 152101 (2018).
[53]L. Freter, "Surface states and Fermi-level pinning on non-polar binary and ternary (Al,Ga)N surfaces," Ph.D. thesis (RWTH Aachen University, Jülich, 2022).
[54]M. S. Miao, A. Janotti, and C. G. Van de Walle, Phys. Rev. B **80**, 155319 (2009).
[55]G. Kresse and J. Furthmüller, Phys. Rev. B **54**, 11169 (1996).
[56]G. Kresse and J. Furthmüller, Comput. Mat. Sci. **6**, 15 (1996).
[57]J. Heyd, G. E. Scuseria, and M. Ernzerhof, J. Chem. Phys. **124**, 219906 (2006).
[58]P. E. Blöchl, Phys. Rev. B **50**, 17953 (1994).
[59]P. Pampili and P. J. Parbrook, Mat. Sci. Semicond. Process. **62**, 180 (2017).